PCCP

PAPER

View Article Online
View Journal

Cite this: DOI: 10.1039/c4cp04017a

Controllable synthesis and SERS characteristics of hollow sea-urchin gold nanoparticles

Junpeng Li,[a] Jun Zhou,*[a] Tao Jiang,[a] Binbing Wang,[a] Min Gu,[b] Lucia Petti[c] and Pasquale Mormile[c]

Received 8th September 2014,
Accepted 16th October 2014

DOI: 10.1039/c4cp04017a

www.rsc.org/pccp

Hollow sea-urchin gold nanoparticles (HSU-GNPs) were successfully prepared through a novel one-step galvanic replacement strategy, and their corresponding optical properties was studied in detail. During the synthesis process, the sizes of the interior hollows of the HSU-GNPs could be changed by adjusting the amount of silver nitrate added into hydrogen tetrachloroaurate trihydrate solution. The absorption spectra of the HSU-GNPs showed that the localized surface plasmon resonance (LSPR) peaks were red-shifted with increasing size of the interior hollows in the HSU-GNPs. When the added amount of silver nitrate was up to 6 μl, the LSPR peak of the synthesized HSU-GNP reached 726 nm as a maximum red-shift. Furthermore, the absorption spectra of the HSU-GNPs with different morphologies were theoretically simulated by the finite element method, which was consistent with the experimental results and explained the origin of the red-shift of the LSPR peaks. In addition, the surface-enhanced Raman scattering (SERS) of the sea urchin gold nanoparticles were also investigated using 4-mercaptobenzoic acid as a Raman reporter molecule. Both the experimental and calculated results showed that the HSU-GNPs had stronger SERS enhancement than the solid sea-urchin gold nanoparticles. In particular, the HSU-GNPs prepared by adding 6 μl silver nitrate exhibited a maximum SERS enhancement factor, EF = 1.1 × 10^9, due to the LSPR peak at 726 nm which is near to the excitation wavelength, 785 nm. This feature is significant for designing a biosensor with a super-high sensitivity based on the morphology of the HSU-GNPs.

1. Introduction

As we know, noble metal nanoparticles (NPs) have special optical properties and are widely applied in the fields of physics, chemistry, biology and life science.[1–8] As a powerful optical functional material, the localized surface plasmon resonance (LSPR) of the noble metal NPs are closely related to their structural parameters, including size, shape, composition, and morphology.[9–11] Thus, the controllable synthesis of noble metal NPs is a very interesting topic and much effort has been devoted to develop the available methods to create metal nanostructures, such as the hydrothermal method, the galvanic replacement method, the oil/water interface method and the template method.[12–15] It is an essential that noble metal NPs with special structures are prepared to manipulate fully their distinctive LSPR properties. In particular, great study has been directed to the design of novel hollow noble metal nanostructures due to their high active surface-to-volume ratio and fascinating applications in numerous areas of optoelectronic imaging, catalysis, environmental monitoring, biosensing, diagnosis and drug delivery.[16–20]

On the other hand, surface-enhanced Raman scattering (SERS) has attracted a great deal of attention because the Raman signal can usually be enhanced by several orders of magnitude for target molecules attached on noble metal surfaces.[21,22] The generation mechanism of SERS is widely recognized as involving two major components: chemical and electromagnetic enhancement. The former component is due to an increased polarizability of the target molecules under the influence of incident radiation, as a result of which new chemical bands with the metal surface are formed.[23,24] The latter component arises from the enhancement of the electromagnetic field for the occurrence of the LSPR of the nanostructured noble metal systems and is highly dependent on matching between the excitation wavelength and the LSPR band.[25,26] As a non-destructive and ultrasensitive spectroscopy analysis technique SERS, originating from electromagnetic enhancement, is more suitable for the detection of biological tissues by using incident radiation in the "window of optical transparency", *i.e.*, in the near infrared (NIR) spectral region of 750–1000 nm.[27,28] Consequence, the LSPR band of the noble

[a] *Institute of Photonics, Faculty of Science, Ningbo University, Ningbo 315211, Zhejiang, China. E-mail: zhoujun@nbu.edu.cn; Fax: +86-574-87600744; Tel: +86-574-87600794*
[b] *Centre for Micro-Photonics, Faculty of Science, Engineering and Technology, Swinburne University of Technology, Hawthorn, VIC 3122, Australia*
[c] *Institute of Cybernetics "E. Caianiello" of CNR, Via Campi Flegrei 34, 80072 Pozzuoli, Italy*

metal nanostructures in such an NIR region possesses obvious superiority and promising applications for biomedical detection.

With regard to the window of optical transparency, we hope that the structure of noble metal NPs can be tailored to satisfy the requirement of its LSPR band close to the wavelength of incident radiation in the NIR region. For example, the LSPR bands of solid spherical gold NPs (GNPs) can be tuned by as much as 50 nm around 520 nm, and the bands of hollow NPs can be continuously adjusted from 500 to 1000 nm by controlling the size of the interior hollows.[29–32] Furthermore, the noble metal nanostructures with rough surfaces have a relatively high SERS intensity because of the existence of "hot spots" (strongly enhanced electromagnetic areas) on the junctions and sharp tips of nanostructures,[33–35] so that great efforts have been directed towards the fabrication of noble metal NPs with various morphologies including raspberries,[36] flowers,[37] meatballs,[38] stars,[39] and sea urchins.[40,41] Thus, a hollow metal nanostructure with a rough morphology is naturally considered to combine their merits, that is, the adjustability of the LSPR band and the high SERS intensity. However, it is a complex chemical process to synthesize a hollow metal nanostructure with rough morphology. Generally, silver seeds should be first be synthesized to build a hollow center in the GNPs,[42] and then the rough morphology of the hollow GNPs are produced by using organic molecules as the capping agent, or stabilizers such as cetyltrimethylammonium bromide (CTAB),[15,43] gum arabic,[38] sodium dodecyl sulfate (SDS),[44] and gelatin protein.[45] A typical sacrificial template approach and the galvanic replacement reaction between Ag NPs and $HAuCl_4$ have been introduced to form hollow GNPs with an urchin-like shell by the aid of ascorbic acid as reducer and polyvinylpyrrolidone (PVP) as dispersant.[46] The introduction of these organic molecules will block the linking of the target molecules to the surface of the GNPs, which inevitably impairs the following SERS applications. Therefore, it is still an enormous challenge to achieve the finely tailored structure of hollow GNPs with sophisticated morphology by a green and simple synthesize process.

In this article, we demonstrate a facile and environmentally friendly galvanic replacement strategy for high-yield synthesis of hollow sea urchin gold nanoparticles (HSU-GNPs). The surface morphologies and internal hollow sizes of the HSU-GNPs were further tuned by altering the added amount of $AgNO_3$. The UV-vis-NIR absorption spectra of the HSU-GNPs with different sizes of interior hollow were experimentally measured and exhibited a tunable red-shift of their LSPR peaks. Meantime, the formation mechanism of the HSU-GNPs was tentatively explained and the origin of LSPR red-shift of the HSU-GNPs was analyzed theoretically by the finite element method (FEM). Lastly, the SERS properties of the HSU-GNPs were investigated by applying 4-mercaptobenzoic acid (4MBA) as a Raman reporter molecule and demonstrated a high SERS enhancement.

2. Experimental

2.1 Chemicals

Silver nitrate ($AgNO_3$) and hydrogen tetrachloroaurate(III) trihydrate ($HAuCl_4 \cdot 3H_2O$) were purchased from Sigma. Ascorbic acid (AA) was purchased from Bodi Chemical Reagent Co. (Tianjin, China). 4MBA was obtained from J&K Chemical. Milli-Q water (18.2 MΩ cm resistivity) was used for all solution preparations. Glassware were cleaned by aqua regia and rinsed with deionized water several times prior to the experiment.

2.2 Synthesis of HSU-GNPs

Four sets of sample solutions were prepared by the following processes: firstly, a different amount of $AgNO_3$ (2, 4, and 6 to 8 μl, 0.1 M) aqueous solutions was injected separately in four glass tubes, and then, for every glass tube, 1 mL of AA (10 mM) aqueous solution and 1 mL of $HAuCl_4$ (3 mM) aqueous solution were quickly injected in turn. After the as-prepared mixed solutions were stirred for 20 seconds, HSU-GNPs solutions were obtained and their color rapidly changed to dark blue.

To obtain the precipitates of HSU-GNPs, the above as-prepared sample solutions were centrifuged at 8000 rpm for 20 min. Then the resultant precipitates were washed with deionized water and absolute ethanol by centrifugation for several times to remove impurities. Finally the four samples of HSU-GNPs were respectively dispersed in 5 mL of deionized water for later experiments.

2.3 Synthesis of 4MBA-tagged HSU-GNPs

20 μl of 4MBA (1 mM) was added to the above purified sample solutions of HSU-GNPs under stirring and the resultant solutions were agitated for 5 h, respectively. Then, the mixed solutions were centrifuged at 9000 rpm for 25 min to remove unbound 4MBA molecules, and the 4MBA-tagged HSU-GNPs settled to the bottom of the reactive vessels. Next, the 4MBA-tagged HSU-GNPs were dispersed in 5 mL deionised water. Lastly, the 4MBA-tagged HSU-GNPs solution were dropped on a quartz glass and air-dried as SERS substrates for further SERS detection.

2.4 Instruments and measurement

Scanning electron microscopy (SEM) and TEM images of the HSU-GNPs were obtained using FESEM (SU-70) at an accelerating voltage of 5 kV and TEM (JEM-2100F JEOL) at an accelerating voltage of 200 kV, respectively. The optical absorption spectra of the HSU-GNPs were recorded with a UV-vis-NIR spectrometer (Cary5000PC). The SERS properties of the HSU-GNPs were examined using a miniature Raman spectrometer (BWS415, B&W Tek Inc.) with a 785 nm semiconductor laser as the excitation source. The measurement parameters of the Raman spectrometer were set as follow: the laser power at the sample position was 49.55 mW and the accumulation time was 5 s; the scattered radiation was collected by a 40× objective lens with numerical aperture (NA) 0.65, dispersed by a grating of 1200 lines per mm, and then passed through a slit with 20 μm width to the charge-coupled device (CCD) (2048 × 2048 pixels) detector. All the analyses were performed at room temperature.

3. Results and discussion

3.1 Characterization of samples

The HSU-GNPs were synthesized by our one-step galvanic replacement method. Typical SEM and TEM images of the HSU-GNPs are

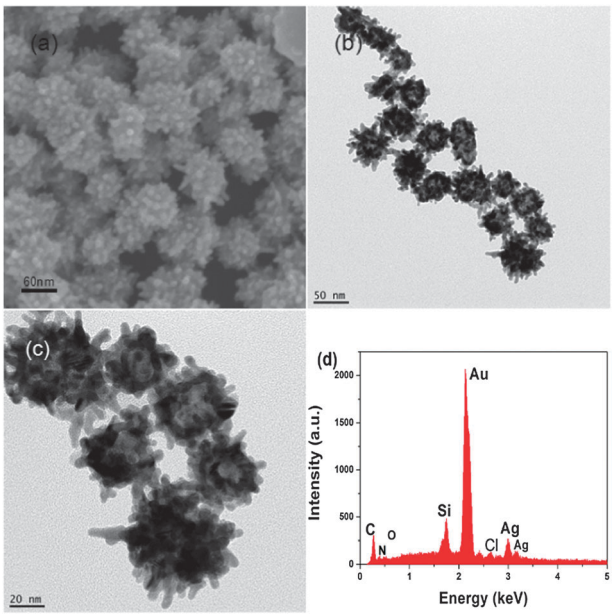

Fig. 1 (a) SEM and (b), (c) TEM images of the HSU-GNPs synthesized with 6 μl $AgNO_3$, (d) EDS of HSU-GNPs.

shown in Fig. 1. From Fig. 1a, the average diameter of the HSU-GNPs was calculated to be 70 ± 5 nm and their tip-lengths in the range of 5–20 nm. Fig. 1b and c show that the HSU-GNPs have distinct interior hollows with sizes ranging from 20 to 45 nm, and the yield of the HSU-GNPs synthesized with 6 μl $AgNO_3$ was determined to be about 80%. The chemical composition of the HSU-GNPs were analyzed by energy-dispersive spectrometry (EDS). As is clearly shown in Fig. 1d, the sample is mainly composed of metallic gold; the elements of silver and chlorine are from the small amount of indiscerptible silver chloride (AgCl) and other elements are from the silica substrate and the derivative of AA.

For insight into the formation mechanisms of the HSU-GNPs, the chemical process of the one-step galvanic replacement synthesis was illustrated in Fig. 2. Conventionally, the synthesis of sea-urchin GNPs involved the template effect of the indiscerptible AgCl introduced by $AgNO_3$ in the $HAuCl_4$ aqueous solution.[46] In the initial reaction solution, Ag^+ and $AuCl_4^-$ existed in the ionic state. Subsequently, the bond of Au–Cl was fractured by the addition of AA so that the Au^{3+} ions were immediately reduced into atoms to form GNPs and the released Cl^- ions combined with Ag^+ ions to produce the indiscerptible AgCl.[47] Then, AgCl would attach to the surfaces of the GNPs as new nucleation cores to aggregate further gold atoms into the sea urchin morphology. However, in our synthesis process of HSU-GNPs, some of the $AgNO_3$ was firstly reduced into Ag atoms to form silver NPs by AA in a short time, and then these silver NPs were mixed with $HAuCl_4$ acting as the reduction center of the gold ions. A galvanic replacement reaction between silver NPs and $HAuCl_4$ lead to the formation of a gold shell around the silver NPs and the dissolution of silver NPs with the migration of electrons. This is because the reduced gold has a great tendency to nucleate on the surfaces of silver NPs to lowering the energetic cost.[42] Along with the disappearance of the internal silver NPs, the external gold shell continually shrank to minimize the surface energy until the complete dissolution of the silver NPs. As a consequence, a hollow gold nanoparticle was obtained. Meanwhile, the same as the above conventional method, the other unreduced Ag^+ ions combined with Cl^- ions to produce the indiscerptible AgCl as the growth director of the thorny GNPs. To understanding the role of $AgNO_3$, a control sample was also prepared by mixing directly AA and $HAuCl_4$ without adding $AgNO_3$. As shown in Fig. 3, only irregular gold nanoclusters were produced in the control sample, which further confirmed the surface-modification effect of indiscerptible AgCl as anchoring sites of the outside branches on suitable surface sites.[47]

According to the above analysis of the synthetic strategy, it is expected that the number of branches and the size ratio of cavity-to-shell can be widely tailored by controlling the amount of $AgNO_3$. As described in Section 2.2, during the preparation of HSU-GNPs, the amount of $AgNO_3$ was selectively regulated from 2 to 8 μl with other synthetic conditions remaining unchanged. The TEM images of four samples were shown in Fig. 4. As shown in Fig. 4a, sample 1 is sea-urchin GNPs with a very little interior hollow, which originate from a low amount of silver NPs. From Fig. 4b and c, there are obvious interior hollows in sea urchin GNPs, *i.e.* samples 2 and 3 are HSU-GNPs, and the interior hollows have grown bigger with increasing amount of $AgNO_3$. Comparing Fig. 4d with Fig. 4c, only a few small hollows appear in sample 4, and the size of the sea urchin GNPs is larger than that of sample 3. This is probably because more-and-more spikes have appeared and have connected to

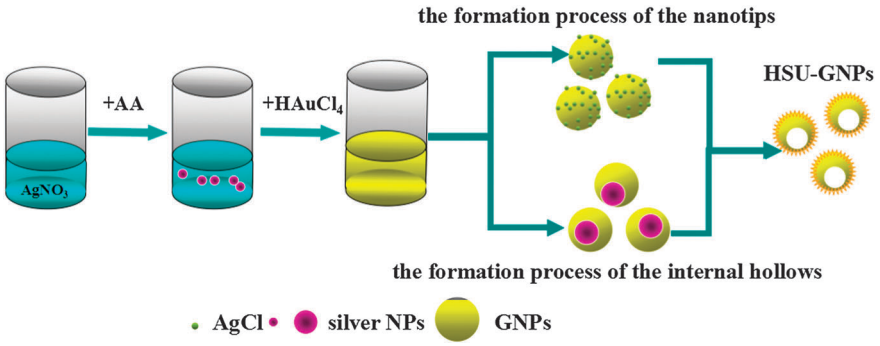

Fig. 2 The chemical process of the one-step galvanic replacement synthesis of the HSU-GNPs.

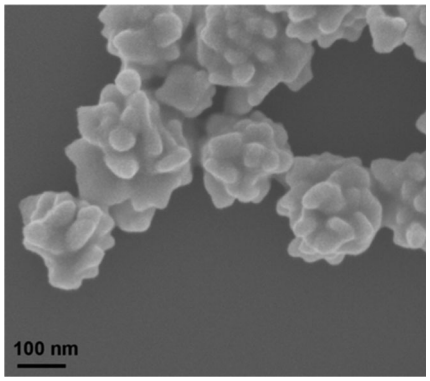

Fig. 3 The SEM image of the GNPs synthesized in the absence of $AgNO_3$.

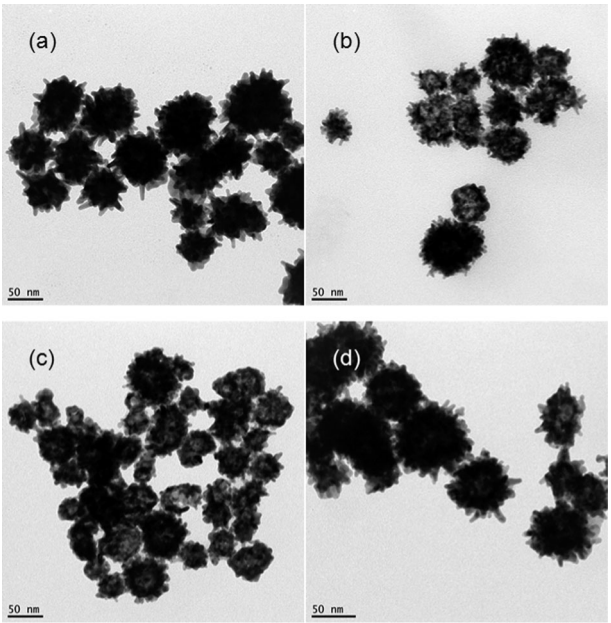

Fig. 4 TEM images of samples prepared with different amounts of $AgNO_3$. (a) Sample 1, 2 μl; (b) sample 2, 4 μl; (c) sample 3, 6 μl; and (d) sample 4, 8 μl.

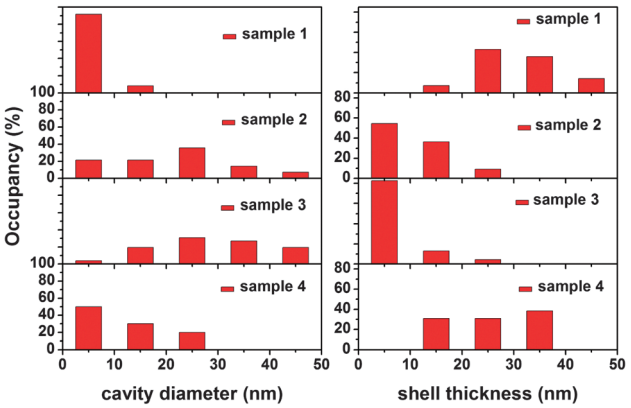

Fig. 5 The cavity size and shell thickness distributions of the different HSU-GNPs samples.

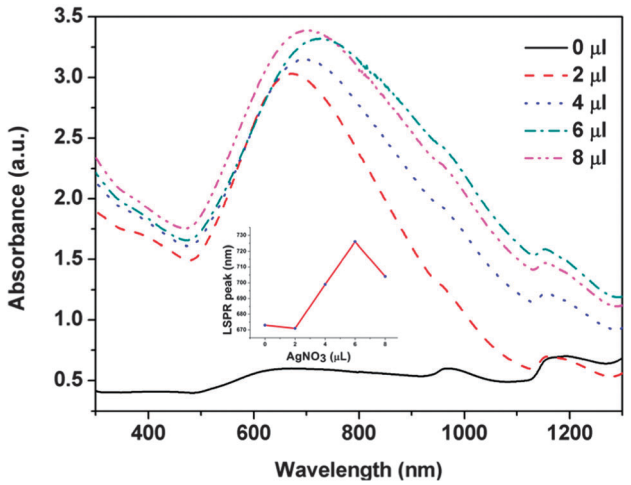

Fig. 6 UV-vis-NIR absorption spectra of GNPs in aqueous solution prepared with different amounts of $AgNO_3$: 0, 2, 4, 6, and 8 μl. The inset is the dependence of LSPR peak on the amount of $AgNO_3$.

each other to form a new layer around the initial gold shell at such an added amount of $AgNO_3$. With the increasing thickness of the new outer layer, the gold shell shrank acutely to minimize the surface energy, which results in the obviously larger GNPs and the smaller hollows. In addition, the cavity size and shell thickness distribution of the HSU-GNPs obtained from various conditions are visually shown in Fig. 5. This clearly presents that the variation of size and morphology of GNPs can be controlled by the amount of $AgNO_3$ which supplied the silver NPs and indiscerptible AgCl in the reaction system. Therefore, the amount of $AgNO_3$ is the crucial factor for the generation of HSU-GNPs.

The UV-vis-NIR absorption spectra of the HSU-GNPs in aqueous solution are shown in Fig. 6. Initially, in the case without added $AgNO_3$, the main LSPR peak of the GNPs locates at 672 nm. With increasing the amount of $AgNO_3$ in the reaction solution, the LSPR peaks of the obtained GNPs gradually shift to the near-infrared wavelength, which derives from the progressive formation of interior hollows and more branches on the rough surfaces of GNPs. When the amount of $AgNO_3$ reached 6 μl, the LSPR peak moves to as far as 726 nm with a broad absorption band from 500 to 1000 nm. However, as shown in Fig. 6, adding $AgNO_3$ up to 8 μl, the LSPR peak undergoes a blue-shift, which shows that the absorption bands of GNPs did not always sustain a red-shift tendency with further increasing the amount of $AgNO_3$ due to the decreasing ratio of hollow-size to shell thickness. Thus, the HSU-GNPs synthesized with 6 μl $AgNO_3$ is selected as our main research objective because its LSPR peak is near the excitation wavelength of the later SERS measurement.

To investigate further the LSPR characteristics' dependence on the structure of HSU-GNPs, the optical absorption spectra of the various sea-urchin GNPs models were simulated using FEM software (COMSOL Multiphysics 4.1). Typically, we set the diameters of the sea-urchin GNPs models to be the same, and their surfaces were textured with some inclined or standard spines, respectively, as illustrated in the inset of Fig. 7. In Fig. 7a, the LSPR peak of the sea urchin GNP with standard spines appears at 781 nm.

However, for the sea urchin GNP with inclined spines, there is a main LSPR peak at 773 nm and two smaller intensity absorption peaks around 900 nm. It is obvious that the two smaller intensity absorption peaks can be attributed to the effect of inclined spikes, which originates from the multipolar plasmon modes induced by the geometric asymmetry of the sea urchin GNP structure.[48] Thus, for the experimental absorption spectra of the sea-urchin GNPs, the small absorption shoulder peak at around 950 nm in Fig. 6 was just the effect of inclined spikes, and the peak located at 1200 nm came from the absorption of aqueous solution. In addition, to verify the red-shift of the LSPR band of the sea-urchin GNPs in Fig. 6, three HSU-GNPs with different thicknesses of nanoshell were also structured. As shown in Fig. 7b, the absorption spectrum of the HSU-GNPs with a nanoshell thickness of 20 nm is almost same as that of the solid sea urchin GNPs (SSU-GNPs). In addition, the LSPR peaks of HSU-GNPs red-shift from 780 nm to 850 nm with the gradual decrease of the nanoshell thickness from 20 nm to 5 nm. It is confirmed that the red-shifts of the absorption bands in Fig. 6 were due to the increase of the hollow sizes in the HSU-GNPs. Actually, as we know, such red-shifts of the absorption bands of HSU-GNPs were caused by the hybridization of the simultaneously excited plasmons on the outer and inner surfaces of a metallic shell. That is, the two excited plasmons will interact to produce a high-energy mode and a low-energy mode which correspond, respectively, to the antisymmetric coupling (antibonding) and the symmetric coupling (bonding) between the cavity and sphere plasmons.[49] When the shell becomes thinner, the interaction of the two plasmons becomes stronger and leads to a larger energy separation between the high-energy mode and the low-energy mode; as a result, a distinct red-shift of the LSPR band occurs. In contrast, for a thick nanoshell, the interaction between the two plasmons is weak and the absorption band does not shift obviously. This is the reason that the absorption spectrum of the HSU-GNP model with a larger shell thickness of 20 nm is coincident with that of the SSU-GNPs model. It should be noted that only one sea-urchin GNP module is used in these calculations. Therefore, the calculated spectra show narrow LSPR bands, which are different from the experimental results because of neglected interactions among the numerous sea urchin GNPs.

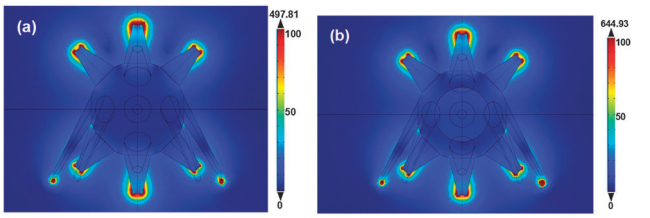

Fig. 8 FEM simulation of the electric field intensity distribution of (a) the SSU-GNPs and (b) the HSU-GNPs with a shell thickness of 10 nm. The diameters of the spheres or shells in the calculated models were same, 50 nm.

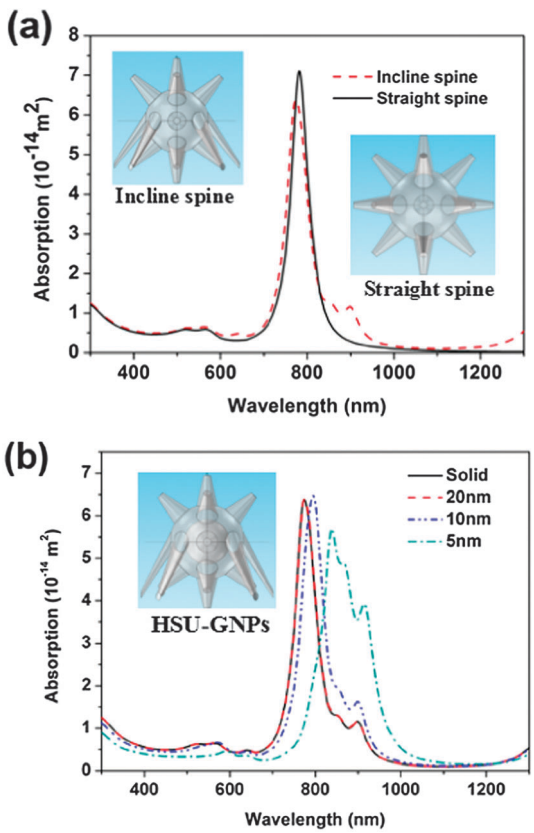

Fig. 7 Simulation absorption spectra of the sea-urchin GNPs with (a) inclined and standard spines and (b) different shell thicknesses. Inset: the models of the sea-urchin GNPs for (a) inclined and straight spines and (b) HSU-GNPs. All calculated models consisted of a sphere with a diameter of 50 nm and sixteen spikes with length 50 nm.

The local electric field intensities around the sea urchin GNPs were calculated to evaluate their performance under irradiation of the monochromatic light at 785 nm. The permittivity data of gold are obtained from the bulk experimental result of Johnson and Christy.[50] The typical distributions of electric field strength around the SSU-GNPs and HSU-GNPs are shown in Fig. 8a and b, respectively. As anticipated, the strongest local electric field areas are observed in the vicinity of the spikes and the maximal electric field intensities are found to be 497.81 and 644.93, respectively. It was found that the HSU-GNPs can produce an enhanced local electric field compared to that of the SSU-GNPs, which indicates the internal hollow of HSU-GNPs is beneficial to enhance the local electric field due to the plasmon hybridization effect discussed above.

3.2 SERS performance of the HSU-GNPs

The SERS performance of the HSU-GNPs was investigated by measuring the Raman spectra of 4MBA-tagged HSU-GNPs. As illustrated in Fig. 9, all the samples of 4MBA-tagged HSU-GNPs present strong characteristic bands of 4MBA due to the exceptional SERS enhancement. The two dominant peaks at 1077 and 1590 cm^{-1} are assigned to the ring-breathing modes.[51] The Raman band at 845 cm^{-1} is attributed to the COO^- bending mode ($\delta(COO^-)$) and that at 1137 cm^{-1} originates from a mixed mode ($13\beta(CCC) + \nu(C–S) + \nu(C–COOH)$).[51,52] Additionally that

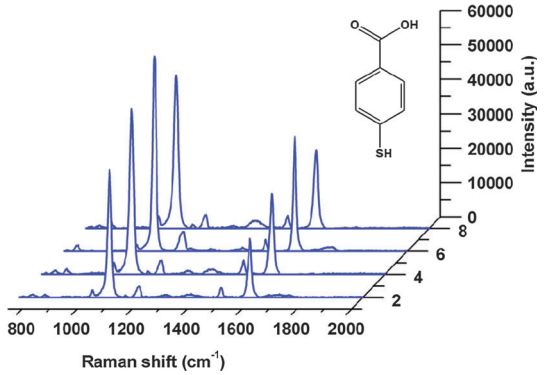

Fig. 9 Raman spectra of 4MBA of the sea-urchin GNPs synthesized with different amounts of $AgNO_3$: (a) 2, (b) 4, (c) 6, and (d) 8 μl.

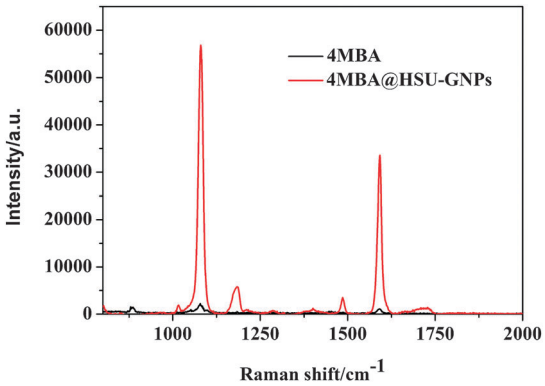

Fig. 10 The SERS spectrum of 4MBA collected from the normal Raman spectrum of 4MBA in solution and the 4MBA-tagged HSU-GNPs under the same sampling conditions.

at 1432 cm^{-1} is ascribed to the $\nu_s(COO^-)$ stretching mode.[53] Although the positions of the Raman peaks of all samples are same, their intensities are different. It can be observed obviously that the intensities of the Raman peaks increased first with increasing amount of $AgNO_3$ and reached a maximum for 4MBA-tagged HSU-GNPs synthesized at 6 μl $AgNO_3$, which possessed the largest interior hollow as described in Section 2.1. Then, the SERS intensities decreased oppositely with the further increase of $AgNO_3$ due to a reduction in the ratio of interior hollow to shell. Thus, the SERS enhancement of the sample synthesized at 6 μl $AgNO_3$ was explored in detail next.

The enhancement factor (EF), which is one of the most important parameters for the SERS effect, was calculated using the following equation:[54–56]

$$EF = (I_{SERS}/I_{bulk}) \times (N_{bulk}/N_{SERS})$$

where I_{SERS} and I_{bulk} are the intensities of the same Raman band in the SERS and bulk Raman spectra, respectively; N_{bulk} is the number of bulk molecules probed in the bulk sample; and N_{SERS} is the number of molecules adsorbed on the SERS substrate. Here, the SERS intensity of the peak at 1076 cm^{-1} was used to calculate the EF value roughly. The Raman spectrum of the 4MBA solution (10 mM) was used to estimate the "bulk" values of the EF. N_{bulk} was calculated by using a 4MBA solution with a concentration at 10 mM and the focal volume of the laser in the Raman system. The diameter of the illumination focus, 1.473 μm, was first calculated using the following equation: diameter = $(\lambda/NA) \times 1.22$,[57] in which the NA of the objective lens of the Raman spectrometer was 0.65 and the wavelength of the excitation laser was 785 nm; besides, the penetration depth of the 785 nm laser beam is about 2 μm in the solutions. The illuminated volume was 1.66 μm^3, and the $N_{bulk} = 1 \times 10^{13}$. To obtain the value of N_{SERS}, with the same diameter of the illumination focus 1.473 μm, $N_{SERS} = 2.3 \times 10^5$ was obtained by dropping 100 μl of a diluted 4MBA-tagged HSU-GNPs solution on a quartz glass with a diameter of 1.5 cm. In addition, as shown in Fig. 10, the I_{bulk} and I_{SERS} (synthesized with 6 μl $AgNO_3$) values (the laser power was 49.55 mW and the accumulation time was 5 s) were 4.27×10^4 and 1.08×10^6, respectively. Thus, the EF value of the SERS substrate was calculated as $EF_{sample3} = 1.1 \times 10^9$. For other samples of the HSU-GNPs synthesized with 2, 4, and 8 μl $AgNO_3$, the calculated EF were $EF_{sample1} = 7.5 \times 10^8$, $EF_{sample2} = 1.03 \times 10^9$ and $EF_{sample4} = 1.02 \times 10^9$, respectively.

The reproducibility of the SERS signal of the 4MBA-tagged HSU-GNPs was also investigated by randomly choosing ten probe sites on the SERS substrates. As shown in Fig. 11a, the

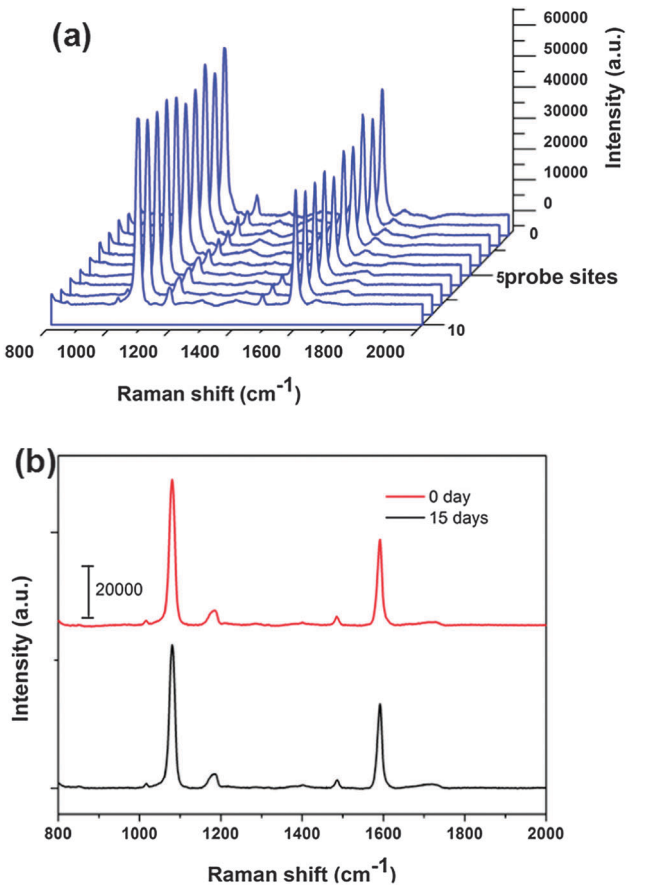

Fig. 11 The Raman spectra of the 4MBA-tagged HSU-GNPs (a) at different probe sites on the SERS substrate, and (b) at different time intervals for the same SERS substrates.

difference among the ten SERS signal intensities is small. These results demonstrated the excellent SERS reproducibility of the SERS substrate. To evaluate the time stability of the SERS signal, the Raman spectra of the 4MBA-tagged HSU-GNPs were measured at different time intervals and are shown in Fig. 11b. This clearly displays the nice time stability of the SERS substrate.

According to the above calculated values of EF, the HSU-GNPs exhibited a high SERS performance. It stems not only from the much higher surface roughness caused by spikes on the surface of GNPs but also the interior hollow in the HSU-GNPs. In fact, as analyzed in Section 3.1, the strongest enhancement of localized electric field areas can be found in the vicinity of the tips of the spikes, which are termed ''hot spots'' to excite SERS up to a higher EF. On the other hand, by comparing the EF values of the four samples, we found that the larger the ratio of interior hollow size to shell thickness the larger the SERS EF values of the HSU-GNPs. The main reason was the better matching of the LSPR band of the HSU-GNPs with the excitation wavelength, which is consistent with the earlier results simulated by FEM.

4. Conclusions

In conclusion, we have developed a facile one-step method to synthesize sea-urchin GNPs with interior hollows for SERS applications. The sizes of the internal cavity as well as the morphologies of the HSU-GNPs can be tuned by altering the added amount of $AgNO_3$. The formation mechanism of the HSU-GNPs is discussed according to the galvanic-replacement synthesis process. Compared the method based on silver seeds, the proposed one-step reaction method is very promising for synthesizing HSU-GNPs. In addition, the UV-vis-NIR absorption spectra of the HSU-GNPs in aqueous solution shows that the main absorption peaks can be shifted to as far as 726 nm by adjusting the ratio of the interior hollow size to shell thickness. The absorption spectra of the HSU-GNPs were simulated numerically by FEM to explore the reason for the red-shifts in the experimental absorption spectra. Furthermore, both the experimental and modulation results show that the SERS enhancement capability of the HSU-GNPs is much better than that of the SSU-GNPs. Therefore, the HSU-GNPs have are superior for SERS applications, which is of great importance for the development of highly sensitive immunoassays.

Acknowledgements

This work was supported by the National Natural Science Foundation of China (NSFC) (Grant No. 61275153, 61320106014 and 11404177); the Natural Science Foundation of Zhejiang (Grant No. LY12A04002); the International Collaboration Program of the Natural Science Foundation of Ningbo (Grant No. 2010D10018 and 2012A610107), and K. C. Wong Magna Foundation of Ningbo University, China. Min Gu acknowledges the support from the Australian Research Council Laureate Fellowship program (FL100100099) and from the Science and Industry Endowment Fund.

Notes and references

1 M. I. Stockman, *Opt. Express*, 2011, **19**, 22029–22106.
2 J. Homola, *Chem. Rev.*, 2008, **108**, 462–493.
3 T. W. Ebbesen, H. J. Lezec, H. F. Ghaemi, T. Thio and P. A. Wolff, *Nature*, 1998, **391**, 667–669.
4 R. M. Jarvis and R. Goodacre, *Chem. Soc. Rev.*, 2008, **37**, 931–936.
5 D. Pissuwan, C. H. Cortie, S. M. Valenzuela and M. B. Cortie, *Trends Biotechnol.*, 2010, **28**, 207–213.
6 Z. Liu, L. Cheng, L. Zhang, Z. B. Yang, Z. Liu and J. X. Fang, *Biomaterials*, 2014, **35**, 4099–4107.
7 J. L. Li, D. Day and M. Gu, *Adv. Mater.*, 2008, **20**, 3866–3871.
8 P. Zijlstra, J. W. M. Chon and M. Gu, *Nature*, 2009, **459**, 410–413.
9 C. L. Nehl and J. H. Hafner, *J. Mater. Chem.*, 2008, **18**, 2415–2419.
10 K. E. Lee, A. V. Hesketh and T. L. Kelly, *Phys. Chem. Chem. Phys.*, 2014, **16**, 12407–12414.
11 C. Noguez and J. Zhang, *J. Phys. Chem. A*, 2009, **113**, 4068–4074.
12 C. Yang, X. T. Su, F. Xiao, J. K. Jian and J. D. Wang, *Sens. Actuators, B*, 2011, **158**, 299–303.
13 J. Han, Y. Liu and R. Guo, *Adv. Funct. Mater.*, 2009, **19**, 1112–1117.
14 H. C. Zeng, *Curr. Nanosci.*, 2007, **3**, 177–181.
15 H. J. You, Y. T. Ji, L. Wang, S. C. Yang, Z. M. Yang, J. X. Fang, X. P. Song and B. J. Ding, *J. Mater. Chem.*, 2012, **22**, 1998–2006.
16 J. Zeng, Q. Zhang, J. Chen and Y. Xia, *Nano Lett.*, 2010, **10**, 30–35.
17 N. D. Zhang, F. Xiao, J. Bai, Y. J. Lai, J. Hou, Y. Z. Xian and L. T. Jin, *Talanta*, 2011, **87**, 100–105.
18 Y. Xia, W. Li, C. M. Cobley, J. Chen, X. Xia, Q. Zhang, M. Yang, E. C. Cho and P. K. Brown, *Acc. Chem. Res.*, 2011, **44**, 914–924.
19 J. Hu, M. Chen, X. Fang and L. Wu, *Chem. Soc. Rev.*, 2011, **40**, 5472–5491.
20 Y. Hu, Q. Chen, Y. Ding, R. Li, X. Jiang and B. Liu, *Adv. Mater.*, 2009, **21**, 3639–3643.
21 J. N. Anker and W. P. Hall, *Nat. Mater.*, 2008, **7**, 442–453.
22 D. C. Rodrigues, G. F. S. Andrade and M. L. A. Temperini, *Phys. Chem. Chem. Phys.*, 2013, **15**, 1169–1176.
23 Y. N. Xia, Y. J. Xiong, B. Lim and S. E. Skrabalak, *Angew. Chem., Int. Ed.*, 2009, **48**, 60.
24 Y. C. Liu, *Langmuir*, 2002, **18**, 174–181.
25 M. T. Sun, S. S. Liu, M. D. Chen and H. X. Xu, *J. Raman Spectrosc.*, 2009, **40**, 137–143.
26 M. Gellner, B. Küstner and S. Schlücker, *Vib. Spectrosc.*, 2009, **50**, 43–47.
27 S. Jeong, N. Won, J. Lee, J. Bang, J. Yoo, S. G. Kim, J. A. Chang, J. Kim and S. Kim, *Chem. Commun.*, 2011, **47**, 8022–8024.
28 J. C. Zhou, Z. L. Yang, W. Dong, R. J. Tang, L. D. Sun and C. H. Yan, *Biomaterials*, 2011, **32**, 9059–9067.
29 Y. G. Sun and Y. N. Xia, *J. Am. Chem. Soc.*, 2004, **126**, 3892–3901.

30 X. Lu, H. Y. Tuan, J. Chen, Z. Y. Li, B. A. Korgel and Y. N. Xia, *J. Am. Chem. Soc.*, 2007, **129**, 1733–1742.
31 D. Schebarchov, B. Auguié and E. C. Le RuD, *Phys. Chem. Chem. Phys.*, 2013, **15**, 4233–4242.
32 D. Aherne, M. Gara, J. M. Kelly and Y. K. Gun'ko, *Adv. Funct. Mater.*, 2010, **20**, 1329–1338.
33 J. Fang, S. Du, S. Lebedkin, Z. Li, R. Kruk, M. Kappes and H. Hahn, *Nano Lett.*, 2010, **10**, 5006–5013.
34 X. Tang, W. Cai, L. Yang and J. Liu, *Nanoscale*, 2014, **6**, 8612–8616.
35 H. Liu, Z. Yang, L. Meng, Y. Sun, J. Wang, L. Yang, J. Liu and Z. Tian, *J. Am. Chem. Soc.*, 2014, **136**, 5332–5341.
36 S. Guo, S. Dong and E. Wang, *Cryst. Growth Des.*, 2008, **8**, 3581–3585.
37 S. Cherevko and C. H. Chung, *Sens. Actuators, B*, 2009, **142**, 216–223.
38 H. Wang and N. J. Halas, *Adv. Mater.*, 2008, **20**, 820–825.
39 W. Moukarzel, J. Fitremann and J. Marty, *Nanoscale*, 2011, **3**, 3285–3290.
40 B. V. Broek, F. Frederix, K. Bonroy, H. Jans, K. Jans, G. Borghs and G. Maes, *Nanotechnology*, 2011, **22**, 015601.
41 J. Li, J. Wu, X. Zhang, Y. Liu, D. Zhou, H. Z. Sun, H. Zhang and B. Yang, *J. Phys. Chem. C*, 2011, **115**, 3630–3637.
42 N. Ortiz and S. E. Skrabalak, *Cryst. Growth Des.*, 2011, **11**, 3545–3550.
43 S. H. Chen, Z. L. Wang, J. Ballato, S. H. Foulger and D. L. Carroll, *J. Am. Chem. Soc.*, 2003, **125**, 16186–16187.
44 C. H. Kuo and M. H. Huang, *Langmuir*, 2005, **21**, 2012–2016.
45 L. H. Lu, K. L. Ai and Y. Ozaki, *Langmuir*, 2008, **24**, 1058–1063.
46 W. Wang, Y. Pang, J. Yan, G. Wang, H. Suo, C. Zhao and S. Xing, *Gold Bull.*, 2012, **45**, 91–98.
47 H. Yuan, W. H. Ma, C. C. Chen, J. C. Zhao, J. W. Liu, H. Y. Zhu and X. P. Gao, *Chem. Mater.*, 2007, **19**, 1592–1600.
48 D. J. Wu, S. M. Jiang, Y. Cheng and X. J. Liu, *Opt. Express*, 2012, **20**, 26559–26567.
49 E. Prodan and P. Nordlander, *J. Chem. Phys.*, 2004, **120**, 5444–5454.
50 P. B. Johnson and R. W. Christy, *Phys. Rev. B: Condens. Matter Mater. Phys.*, 1972, **6**, 43–70.
51 A. Michota and J. Bukowska, *J. Raman Spectrosc.*, 2003, **34**, 21–25.
52 Y. J. Kwon, D. H. Son, S. J. Ahn, M. S. Kim and K. Kim, *J. Phys. Chem.*, 1994, **98**, 8481–8487.
53 M. Wells, D. L. Dermody, H. C. Yang, T. Kim, R. M. Crooks and A. J. Ricco, *Langmuir*, 1996, **12**, 1989–1996.
54 E. C. L. Ru, E. Blackie, M. Meyer and P. G. Etchegoin, *J. Phys. Chem. C*, 2007, **111**, 13794–13803.
55 G. Hong, C. Li and L. Qi, *Adv. Funct. Mater.*, 2010, **20**, 3774–3783.
56 Y. He, S. Su, T. T. Xu, Y. L. Zhong, J. A. Zapien, J. Li, C. H. Fan and S. T. Lee, *Nano Today*, 2011, **6**, 122–130.
57 S. P. Xu, X. H. Ji, W. Q. Xu, X. L. Li, L. Y. Wang, Y. B. Bai, B. Zhao and Y. Ozaki, *Analyst*, 2004, **129**, 63–68.

